Title
Neuromodulatory control of localized dendritic spiking in critical period cortex.

Journal
Nature, 567(7746)

ISSN
0028-0836

Authors
Yaeger, Courtney E
Ringach, Dario L
Trachtenberg, Joshua T

Publication Date
2019-03-01

DOI
10.1038/s41586-019-0963-3

Peer reviewed

Published in final edited form as:

Nature. 2019 March ; 567(7746): 100–104. doi:10.1038/s41586-019-0963-3.

Neuromodulatory control of localized dendritic spiking in critical period cortex

Courtney E. Yaeger[1], **Dario L. Ringach**[1,2], and **Joshua T. Trachtenberg**[1]

[1]Department of Neurobiology, David Geffen School of Medicine at UCLA, Los Angeles, CA USA

[2]Department of Psychology, University of California, Los Angeles, CA USA

Abstract

Sensory experience in early postnatal life, during so-called critical periods, restructures neural circuitry to enhance information processing. It is unclear why the cortex is susceptible to sensory instruction in early life and why this susceptibility wanes with age. Here, we define a developmentally-restricted engagement of inhibitory circuitry that shapes localized dendritic activity and is needed for vision to drive the emergence of binocular visual responses in mouse primary visual cortex. We find that at the peak of the critical period for binocular plasticity, acetylcholine released from the basal forebrain during periods of heightened arousal directly excites somatostatin-expressing (SST) interneurons. Their inhibition of pyramidal cell dendrites and of fast-spiking, parvalbumin-expressing (PV) interneurons enhances branch-specific dendritic responses and somatic spike rates within pyramidal cells. By adulthood, this cholinergic sensitivity is lost, and compartmentalized dendritic responses are absent but can be re-instated by optogenetic activation of SST cells. Conversely, suppressing SST cell activity during the critical period prevents the normal development of binocular receptive fields by impairing the maturation of ipsilateral eye inputs. This transient cholinergic modulation of SST cells, therefore, appears to orchestrate two features of neural plasticity – somatic disinhibition and compartmentalized dendritic spiking. Loss of this modulation may contribute to critical period closure.

A major and unanswered question is what distinguishes the engagement of plasticity during critical periods of early postnatal development from that in adult cortex. In adult cortex, the necessary components of plasticity include attention and/or reinforcement[1], disinhibition of pyramidal cell bodies[2,3], and various forms of dendritic potentiation, including localized dendritic spiking[4,5,6]. Less is understood about the engagement of plasticity in the

Correspondence and requests for materials should be addressed to joshua.trachtenberg@gmail.com.

Author Contribution: C.E.Y., D.L.R., and J.T.T. conceived of the experiments and performed data analysis. C.E.Y. carried out all of the experiments and all of the statistical analyses. D.L.R. wrote all of the software for 2-photon acquisition, image alignment, cell identification, and temporal deconvolution. D.L.R. and J.T.T. provided oversight of the project. C.E.Y. and J.T.T. wrote the paper and prepared the figures.

Competing Interests: J.T.T. is a co-owner of Neurolabware LLC.

DATA AVAILABILITY

The data sets generated during and/or analyzed during the current study are available from the corresponding author on reasonable request.

developing cortex, where sensory experience exerts an extremely robust and permanent influence on cortical circuitry. Neuromodulation and inhibition are key players in this plasticity[7,8,9], but their joint influence on dendritic integration and somatic firing in pyramidal cells is not known. Dendritic compartmentalization is particularly relevant to the establishment of binocular receptive fields in primary visual cortex, which depends on a strengthening of initially weak, subthreshold ipsilateral eye input[10,11] and the matching of their receptive field tuning properties to the contralateral eye[12]. Local dendritic spiking would enhance this process, driving the functional clustering of synaptic inputs[13,14] as well as the potentiation of weak, but coactive inputs[15–17]. To obtain a more informed understanding of how vision drives plasticity during critical periods and why this influence is lost with age, we investigated the modulation of pyramidal neurons and the three major types of inhibitory neurons in primary visual cortex: dendrite-targeting SST cells, soma-targeting PV cells, and cells expressing the vasoactive intestinal peptide (VIP)[18]. We gauged cell type-specific changes in activity as a function of neuromodulation by imaging spontaneous and visually-evoked changes in fluorescence of the genetically-encoded calcium indicator GCaMP6 via resonant scanning 2-photon microscopy. These measures were made in alert, head-fixed mice running or resting on a spherical treadmill. Measurements were taken at two developmental ages – 4 weeks of age (postnatal day 28; P28) and 8 weeks of age (postnatal day 56; P56). P28 is the age of greatest sensitivity to the instructive influence of vision, and P56 is well beyond critical period closure[19], in addition to being a commonly used age of study for adult mice.

At P28, the spontaneous activities of SST cells increased during periods of locomotion, but by P56 this positive correlation was significantly reduced (Fig. 1a–b). Visually-evoked responses of SST cells followed a similar trend. At P28, the median change in visually-evoked GCaMP6s fluorescence was larger during locomotion than during rest, and by P56 this state-dependence was absent (Fig. 1c–d, Extended Data Fig. 1). These measures suggest that there is an age-dependent loss in the sensitivity of SST cells to neuromodulators released into cortex during running, because the reticular activating system is engaged during locomotion[20,21]. We tested this hypothesis in acute cortical slices by measuring evoked firing rates of SST cells in layer 2/3 of primary visual cortex to the cholinergic agonist carbachol. Supporting earlier work[22–24], we found that P28 SST cells responded robustly to carbachol (2mM, bath application) when synaptic signaling of local excitatory and inhibitory neurons was blocked. Notably, this direct cholinergic response was not present at P56, despite unchanged intrinsic properties (Fig. 1e–f, Extended Data Fig. 2). Expanding on these results *in vivo*, we found that optogenetic stimulation of cholinergic cells in the basal forebrain drove time-locked GCaMP6s responses in SST-cells in visual cortex of P28, but not P56 mice (Fig. 1g–j). Collectively, these measures indicate that at the peak of the critical period – and not in adulthood – SST cell responses are enhanced by acetylcholine released from basal forebrain cortical projections.

Because SST cells primarily receive inhibition from VIP cells[18,25,26], we also measured VIP interneuron activity at both developmental time points. No age-dependent changes in the influence of behavioral state or sensitivity to carbachol were observed on VIP cell responses (Extended Data Fig. 3), consistent with prior findings[22,24,27]. Presumptive VIP input to SST cells also appeared to be constant with age: in acute slices of binocular vision cortex,

carbachol-mediated inhibitory currents were evident in SST cells at both ages with similar amplitudes (Extended Data Fig. 4).

SST interneurons send inhibitory input to all other cell types, including fast-spiking PV cells[25,28]. When we examined spontaneous responses of PV cells, we found no influence of locomotive state in P28 mice; by P56, however, PV responses increased when mice ran (Fig. 2a–b). Similarly, running enhanced visually-evoked PV cell responses at P56, but not at P28 (Fig. 2c–d). This increase at P56 is unlikely to be caused by direct actions of acetylcholine on PV cells, as whole-cell recordings from PV cells in acute cortical slices showed no direct responses to carbachol at either P28 or P56 (Fig. 2e–f). This is consistent with prior studies, which show that the modulation of PV responses is indirect[22,24,27]. Supporting this view, carbachol induced large GABA-mediated inhibitory currents in PV cells at P28 but not at P56 (Fig. 2g–h). These measures indicate that cholinergic action on SST cells and VIP cells drive a strong inhibition of PV cells at P28, but by P56, this inhibition is lessened – a developmental shift opposite to what we found in SST cells.

Given these reciprocal differences of the most prominent sources of inhibition to pyramidal neurons, an intriguing question is whether arousal state differently impacts visually-evoked dendritic and somatic responses in critical period versus adult mice. In adult cortex, branch-specific dendritic activity arises during active learning and decision making, and these localized responses facilitate compartmentalized synaptic plasticity[4,5]. With this in mind, we measured visually-evoked dendritic Ca^{2+} responses (GCaMP6f) along the apical dendrites of layer 2/3 pyramidal neurons from both age groups. We recorded from sister dendrites, in which a bifurcation from a parent dendrite was identifiable within the imaging plane. Calcium signals were extracted from dendritic branches and temporally deconvolved, giving a measure proportional to spike rate in arbitrary units[29] (Fig. 3a–b). While deconvolution has not been validated physiologically for dendritic calcium transients, measures of dendritic calcium transients, spiking, and membrane potential are strongly correlated[30]. A comparison of the results obtained by processing the raw fluorescence signal is presented in Extended Data Fig. 5. At both ages, dendritic activity increased when mice ran (Fig. 3c), but at P28, running also drove a decorrelation in the activity of sister branches – an effect not seen at P56 (Fig. 3d–e, Extended Data Fig. 6). In measures from pyramidal cell somas, putative spike rates increased more during locomotion at P28 than at P56 (Fig. 3f–h). Thus, age-dependent changes in pyramidal cell activity reflect changes in inhibitory drive from SST and PV cells. Notably, pyramidal cell responses only showed this age-dependent shift when processing visual information; changes in spontaneous responses as a function of locomotion and age were not measurably different (Extended Data Fig. 7).

Emergent from these measures is a hypothesis in which cholinergic enhancement of SST cell activity during the critical period drives branch-specific dendritic activity and disinhibition in pyramidal cells. To test this hypothesis, we artificially enhanced SST cell activity in adult cortex, where SST activity is relatively lower than during the critical period, and examined the impact on dendritic and somatic activity. In control studies in which SST cells expressed channelrhodopsin (ChR2), blue light pulses of 10 ms duration at 15 Hz reliably drove SST cell responses (Extended Data Fig. 8). With this established, we expressed ChR2 in SST cells and GCaMP6f in pyramidal neurons in adult mice to determine

if optogenetic stimulation of SST cells impacted dendritic responses (Fig. 4a). Evoked activities of sister dendrites were recorded across periods of movement and rest to obtain a baseline level of dendritic activity and sister branch covariance. Under baseline conditions, sister dendrites in adult cortex behaved as in Figure 3: calcium responses increased during periods of movement, and stimulation did not affect overall activity levels (Fig 4b). However, upon optogenetic stimulation of SST cells, branch-specific dendritic activity re-emerged, though only when mice were running (Fig. 4c,d; see discussion). Responses of pyramidal cell somas were also elevated over baseline during SST stimulation and running (Fig. 4e–g).

To explore whether enhanced SST cell activity seen at P28 impacts critical period plasticity in the typically developing cortex, we chronically suppressed SST cell activity during the critical period via hM4Di-DREADD receptors and measured the effect on the emergence of binocularly-matched receptive field tuning in pyramidal neurons – the most salient consequence of critical period plasticity in the visual cortex[12]. In SST cells expressing DREADD receptors, intraperitoneal injection of CNO (2.5 mg/kg) caused a significant reduction in evoked amplitude over an 8-hour timespan (Extended Data Fig. 9). In mice with DREADDs selectively expressed in SST cells and GCaMP6f in pyramidal neurons, we administered CNO from P24 through P27 and then measured binocular neuron tuning in the orientation and spatial frequency domains at P28. Tuning of contralateral inputs was unaffected by SST suppression, but inferred spike rates increased (Fig. 5a–c). By contrast, ipsilateral eye inputs were degraded by both measures (Fig. 5d–f). Moreover, receptive field tuning between contralateral and ipsilateral inputs was poorly matched (Fig. 5g–h).

The data we present here reveal a transient circuit linking cholinergic neuromodulation and inhibition, which act in unison with vision to shape cortical circuitry during the critical period. In this circuit, acetylcholine released from basal forebrain into cortex during periods of heightened arousal directly activates SST cells, resulting in branch-specific dendritic inhibition and somatic disinhibition – two hallmarks of cortical plasticity[2–4,8]. The presence of local calcium activity within functionally distinct dendritic compartments and enhanced somatic spiking may be the substrate through which sensory experience engages plasticity in the very young cortex. The engagement of these components is distinct from adult cortex, where these properties emerge during learning and decision-making[4,5] – states that involve attention and reinforcement.

Notably, direct stimulation of SST cells in adult cortex was not sufficient to drive an increase in branch-specific dendritic activity and somatic spiking. These events only occurred when SST stimulation was concurrent with running. One possibility is that acetylcholine acts in parallel on SST cells and pyramidal cells to evoke compartmentalized dendritic plasticity in the developing cortex. Local dendritic activity, backpropagations, and acetylcholine combined have powerful implications for inducing plasticity within specific dendritic compartments[16,17] and could strengthen initially weak inputs in developing cortex. The loss of the cholinergic co-activation of excitatory cells and SST-mediated inhibition would shift plasticity rules, in which inhibition becomes inverted along the somatodendritic axis, and may play a role in the closure of the critical period.

METHODS

Animals

All procedures were done in compliance with the Office of Animal Research Oversight, the Institutional Animal Care and Use Committee, at the University of California, Los Angeles. Cre lines were used to selectively express GCaMP6 in specific cell types. The following mouse lines were used from Jackson Laboratories: SST-IRES-Cre (stock no. 018973), PV-Cre (stock no. 08069), VIP-IRES-Cre (stock no. 010908), and ChAT-Cre (stock no. 006410). For optical identification of interneurons, mice were crossed with Ai9-expressing mice (stock no. 007905). All mice were heterozygous for their respective transgenes, and both male and female mice were used. Mice were group housed under a normal 12/12 light-dark cycle.

Cranial window surgeries

All two-photon imaging was carried out through a cranial window. For all ages, surgical preparation included administration of anti-inflammatory Carprofen, the affixation of an aluminum headbar to the skull, the removal of bone over the primary visual cortex, injection of viral vectors, and the placement of a glass coverslip over the exposed region. Body temperature was maintained at 37°C. Under isoflurane anesthesia, the scalp was retracted and Vetbond was used to coat the skull surface and the edges of the exposed area, followed by a layer of black dental acrylic. The aluminum headbar was affixed with dental acrylic to this surface, caudal to the area of interest over V1. A 3 mm-diameter area over V1 (centered at 1.5 mm from bregma and 3 mm from the midline) was removed using a high speed drill. Following virus injection, the craniotomy was sealed with coverglass using Vetbond to create an imaging window. All remaining exposed regions of skull and surgery margins were sealed with Vetbond and acrylic. Animals were given a one-week period or more for recovery before imaging. For adult mice, injections and surgeries were performed altogether, 2 weeks prior to imaging at P56. For imaging at P28, mice were injected with virus via a small burrhole over V1 at P14, with the headbar and craniotomy surgeries performed at P21.

Virus injections

For calcium imaging, either CaMKII-GCaMP6 or flex-GCaMP6s (UPenn Vector Core: AAV1.CamKII.GCaMP6f.WPRE.SV40, number AV-1-PV3435, and AAV1.Syn.Flex.GCaMP6s.WPRE.SV40, number AV-1-PV2821) were expressed in cortical neurons (titer: 10^{13} genomes/ml). For all age groups, virus was injected 2 weeks prior to imaging. Virus injection was done using a glass micropipette and a PicoSprizer III (Parker) (15 p.s.i., 10 ms pulses, 3 s between pulses). For imaging Cre-dependent interneuron classes, virus containing flex-GCaMP6s was used, injected at a beginning depth of 350 μm and moving up every 50 μm, with the last injection depth being 100 μm below the pial surface, for a total of approximately 1.5 μL of injected virus across cortical layer 2/3. For imaging pyramidal cell dendrites, a viral vector containing CaMKII-GCaMP6f was used, and approximately 50 nL of undiluted virus was injected at a depth of 300 μm from the cortical surface in the center of V1. The low volume for these experiments was beneficial to achieving optimal sparsity for observing pyramidal cell processes. For optogenetic experiments, flex-ChR2 (AAV1.CAGGS.Flex.ChR2-tdTomato.WPRE.SV40, number AV-1–

18917P, titer: 10^{13} genomes/ml) was used in multiple Cre-dependent lines. For stimulating SST cells in V1, flex-ChR2 and GCaMP6s were expressed in SST neurons expressing Cre. Injections were done as for interneuron populations, but with a 1:1 ratio of each virus (approximately 0.75 μL of each). For pyramidal cell imaging with SST cell activation, flex-ChR2 and CaMKII-GCaMP were injected in 3–50nL injections as stated above, with viruses mixed in a 1:1 ratio. For optogenetic manipulation of the nucleus basalis, flex-ChR2 was injected at coordinates of 1.8mm lateral and 0.5mm posterior to bregma, at a depth of 4.3mm, at a volume of approximately 0.5 μL. For experiments using inhibitory DREADDs, a Cre-dependent virus was used (AAV2.hSyn.DIO.hM4D(Gi).mCherry, number 44362-AAV2, Addgene, titer 7×10^{12}genomes/ml) and mixed with flex-GCaMP6s at a 2:1 ratio to account for the lower titer of the DREADD-containing virus. Approximately 1–2 μL were injected into V1. For binocular matching experiments, CaMKII-GCaMP6f and flex-DREADD were co-injected at the same ratio and volume at P10, and craniotomies were performed as usual at P21. All animals were given 2 weeks before imaging for sufficient virus expression.

Two-photon calcium imaging and visual stimulation

Calcium responses of specific cell types and processes were acquired using a resonant-scanning two-photon microscope (Neurolabware) controlled by Scanbox acquisition software. A Coherent Discovery laser (Coherent Inc.) was used for GCaMP excitation, fixed at a wavelength of 920 nm. The objective used was a 16x water-immersion lens (Nikon, 0.8NA, 3 mm working distance). Image sequences were captured at 15.5 Hz at a depth of 100–300 microns below the pia. A dichroic mirror (Semrock) was used to separate red and green fluorescence: for red fluorescence detection, the laser wavelength was adjusted to 1000 nm. All testing was done with awake, head-fixed mice that were free to move on a spherical treadmill. Prior to testing, mice underwent at least two days of training to acclimate to the treadmill and head-fixation. Treadmill movement was captured by a Dalsa Genie M1280 camera (Teledyne Dalsa), which was synchronized to microscope scanning. Visual stimuli were presented on a large LCD monitor directly in front of the animal and 18 cm from the eye. Visual stimuli consisted of nonrepeating natural movies with intermittent gray screens (9s on, 14s off). Spontaneous response data was collected with a blank gray screen. For measuring receptive field properties, the binocular zone was identified using a sparse noise visual stimulus which revealed the amount of neuronal activity at the center of the visual field. Following localization, ipsilateral and contralateral inputs to binocular neurons were recorded with an opaque patch placed immediately in front of the eye to temporarily occlude visual input. Evoked responses were then recorded using a random sinusoidal grating, varying in orientation (0–170 degrees) and spatial frequency (0–0.15 cycles/degree) was presented at 4 Hz for a total of 15 minutes.

Analysis of two-photon imaging data

Collected data was processed using the following pipeline provided by Scanbox software: Recorded frames were aligned with a recursive Lucas-Kanade algorithm. Regions of interest were created in a semi-automated manner, in which correlation coefficients among pixels could be thresholded and used to dictate areas of significant activity. Neuropil-subtracted signals were extracted from these regions of interest, and signals were deconvolved using the

Vanilla algorithm, which is a linear filter with a static nonlinearity. The parameters of the temporal filter and static nonlinearity were determined by maximizing the correlation of the deconvolved signal with neuronal spiking from a community-contributed database[29].

For all correlation analyses, Spearman's correlation coefficient was used. For comparisons of amplitude, the median response in ΔF/F was determined as outlined in Extended Data Figure 1. In some cases, comparisons were normalized to give a percentage. For calculating fold change in dendritic calcium events, we took the ratio of event probabilities between sister branches, performed a log-transformation, and took the absolute value.

For receptive field analyses, a spatiotemporal kernel was computed for each cell based on the average responses to the randomized grating and smoothed with a Gaussian filter. Signal to noise for each kernel was determined by taking the maximum response divided by the mean. Binocular neurons were classified by SNRs greater than 1.5 for both ipsilateral and contralateral-driven responses. The orientation preference was determined by calculating the circular variance, and the difference between preferred orientations of ipsilateral and contralateral inputs is given by Δθ, in degrees.

In vivo optogenetic manipulations of SST cells or nucleus basalis

For full-field stimulation of SST cells in V1, a high-power LED (ThorLabs) with a blue-light filter (470 nm, Semrock) was added to the two-photon pathway. LED intensity was a maximum of 10 mW mm^{-1} at the center of the cranial window surface, which was measured by a power meter (Thorlabs). LED triggering was synced to laser scanning through Scanbox, and activation of the LED silenced a gated photomultiplier (Hamamatsu) prior to LED light delivery, so that light from the LED was not collected and the integrity of the PMT was preserved. Blue light was delivered in 10ms pulses, repeated 25 times at 15Hz. Stimulation was done during both periods of stillness and movement, and when done within the same imaging session, at least 30 seconds was left between stimulation periods.

To selectively stimulate ChAT-positive neurons and axons from the nucleus basalis, mice were generated to express Cre in SST cells and also in neurons expressing choline acetyltransferase (ChAT), an enzyme responsible for the synthesis of acetylcholine. In each mouse, a local injection of a flexed channelrhodopsin (ChR2) was made into nucleus basalis and, separately, flexed-GCaMP6s was injected into visual cortex. While neurons expressing ChAT or SST are present in both areas, SST neurons of the basal forebrain do not project to cortex[31], and cortical ChAT-positive neurons make up less than 1% of all cortical interneurons[32]. A fiber-optic cannula (Prizmatix) was implanted unilaterally one to two weeks prior to imaging, following virus injections. Cannulae were 4.3 mm long and were inserted at a 30-degree angle (2mm rostral of injection site) to allow space for the objective and were approximately 0.5 mm away from the nucleus basalis. Similar to full-field stimulation experiments in V1, blue light (~460nm) was administered in 10ms pulses, 25 times at 15 Hz at 5–6 mW. To minimize any natural activation of the basal forebrain during these experiments, mice were trained to be motionless and observed a gray screen throughout recordings.

DREADD manipulation of SST cells during development

To suppress SST cell activity over a prolonged period during development, we used a Cre-dependent inhibitory DREADD (hM4Di) in SST-Cre mice. To initially validate DREADD-mediated suppression of SST interneurons, flexed GCaMP6s and DREADDs were co-expressed in SST cells. Following the craniotomy and a period of recovery, evoked activity of SST cells was recorded using natural movie scenes. CNO (C0832, Sigma Aldrich) was dissolved in saline to make a 0.5 mg per ml solution, containing 0.5% DMSO to prevent separation. After baseline recordings, CNO was administered via intraperitoneal injection at a dose of 0.10 ml per 20 g body weight, or 2.5 mg/kg. 2 hours after injection, the same SST cells were reimaged. This procedure was repeated at 4 and 8 hours to determine how long the effect lasted. In a separate group, CNO was administered to mice without DREADD expression to determine any unexpected effects of clozapine on SST cells.

For experiments in which SST cell activity was suppressed for a period of days, hM4Di DREADDs were expressed in SST cells concurrently with GCaMP6f in pyramidal neurons. This was accomplished by injecting flexed DREADD along with CaMKII-GCaMP6f in the binocular zone of primary visual cortex in SST-Cre mice at postnatal day 10 and allowed 2 weeks for expression. Craniotomies were performed on P21, and mice received CNO (2.5 mg/kg) every 8–12 hours from P24-P27. 12 or more hours from the last dose of CNO, the ipsilateral and contralateral inputs to binocular neurons were tested. Control groups, either expressing DREADD and receiving saline, or not expressing DREADD and receiving CNO, underwent the same procedure.

Acute slice preparation

Whole cell recordings were done in acute slices from P28 and P56 mice. tdTomato-expressing mouse lines (SST-Cre/Ai9 mice; PV-Cre/Ai9; VIP-Cre/Ai9) were used for targeting specific interneuron subtypes. Animals were anesthetized with isoflurane and perfused with ice-cold sucrose-ACSF. 300 μM-thick coronal slices from the visual cortex were cut on a vibratome in ice-cold sucrose-ACSF solution. Slices were incubated in regular ACSF for 30 minutes at 25 degrees Celsius prior to recording at room temperature. Sucrose-ACSF was perfused with carbogen and contained (in mM): sucrose, 222; glucose, 11; NaHCO3, 26; NaH2PO4, 1; KCl, 3; MgCl, 7; and CaCl, 0.5. Regular ACSF contained (in mM): sucrose, 4; MgCl, 2; CaCl, 2.5; and NaCl, 124. A low-chloride K-gluconate intracellular pipette solution was used to record cells in current clamp mode, containing (in mM): K-gluconate, 126; KCl, 4; HEPES, 10; ATP-Mg, 4; GTP-Na, 0.3; and Na-phosphocreatine, 10; pH 7.4, 300 mOsm. A high-chloride internal solution was used to record IPSCs in voltage clamp mode, containing (in mM): KCl, 120; HEPES, 10; Mg-ATP, 4; GTP-Na, 0.3; and Na-phosphocreatine, 10; pH 7.4, 295 mOsm. Cholinergic responses were tested through bath application of cholinergic agonist carbachol (CCh, 2mM), in which CCh was added in small amounts (0.3–0.5μL). Excitatory and inhibitory synaptic activity were blocked using bath-applied CNQX (10μM) and GABAzine (10μM).

Intracellular recording and analysis

Cells in layer 2/3 were visualized with an Olympus BX61WI microscope coupled with a 40× water immersion lens (Olympus), infrared-DIC optics and CCD camera (Qimaging).

Slices were screened for cell bodies containing tdTomato using a custom fluorescence filter. Glass pipettes (4 −7 MΩ) were pulled with a Sutter Instruments P1000 puller. Data was collected and acquired with a MultiClamp 700B amplifier and a Digidata 1440A system (Molecular Devices), with WinWCP software (Strathclyde). For all cells, response to current steps, input resistance, and access resistance was measured before drug application and after washout (>30min) to verify the health of each cell. Only cells without significant changes in current-step responses were used for further analysis (Extended Data Fig 2). Firing rate and changes in membrane potential were analyzed using Clampfit software.

Statistics

All statistical analyses were done using non-parametric procedures in Matlab. Significance levels were set to $\alpha < 0.05$ for all two-group comparisons. Mann-Whitney U tests were employed for testing differences between independent groups, while groups with repeated measures were compared with the Wilcoxon signed-rank test. In comparisons involving more than two groups, custom written Matlab code was used to tailor an ANOVA to non-normally distributed data with unequal variances, for independent and non-independent groupings: F-statistics were computed as the ratio between sum of squares among groups and sum of squares within groups, and p-values were calculated by comparing the F-statistic derived from the data and the average F-statistic generated from resampling the shuffled data 10,000 times. Our data required 2 types of ANOVAs: 2-way ANOVA with repeated measures and one-way ANOVA with repeated measures (Kruskal-Wallis test). ANOVAs were followed by post-hoc comparisons with either the Wilcoxon signed-rank test or the Mann-Whitney U test where justified. The Bonferroni method was used to correct for multiple comparisons.

Extended Data

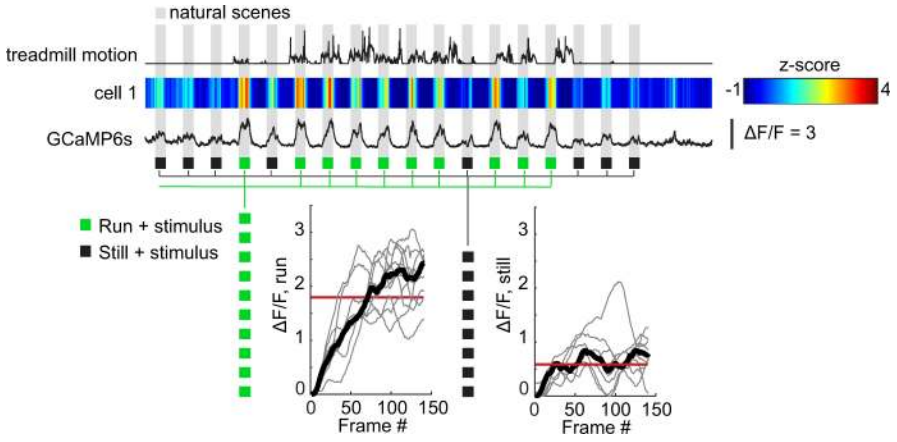

Extended Data Fig. 1 |. Analysis of ΔF/F during still or run events.

Example P28 SST cell GCaMP6s responses during natural scenes with variable running activity. Treadmill motion and corresponding GCaMP6s signal is shown (15.5 fps), with grey bars denoting periods of visual stimulation. Z-score of GCaMP signal is denoted by the colormap, and the trace denotes ΔF/F. Each presentation of the visual stimulus is classified as either a run (green) or still (black) trial. ΔF/F of GCaMP6s from all run (left) or still

(right) trials are plotted. The median (red) of the median (black) ΔF/F response is taken to give an average value for still or run trials.

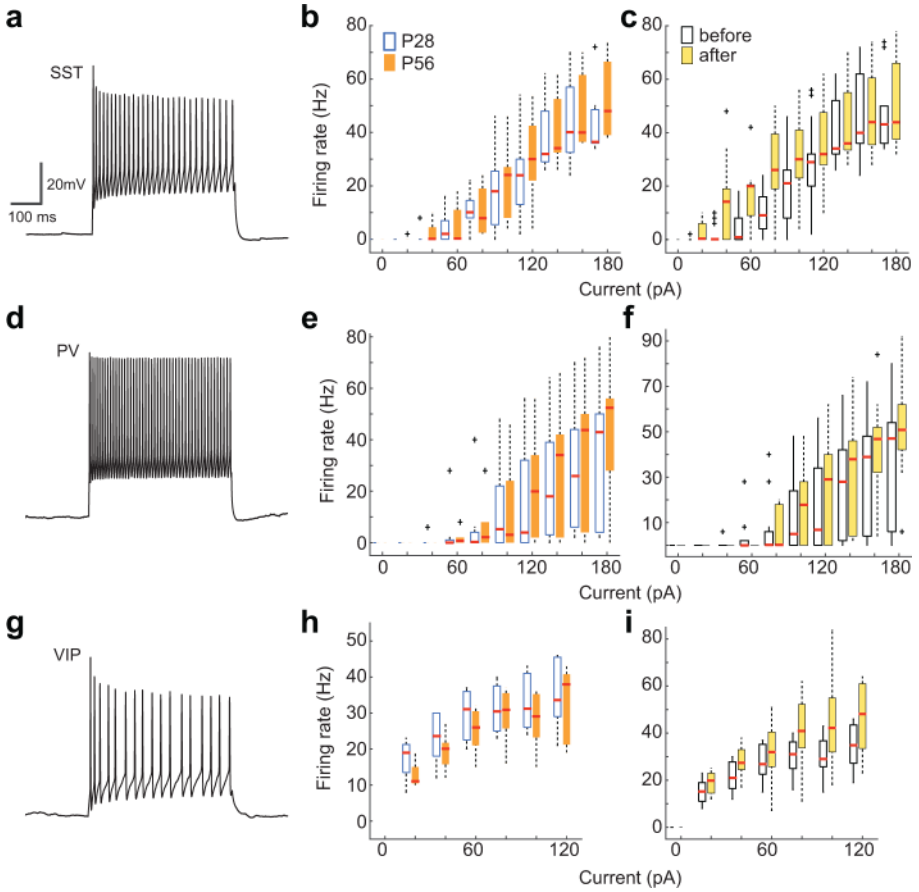

Extended Data Fig. 2 |. Current injection responses for SST, PV, and VIP cells before and after carbachol application.

a, Example current injection responses showing distinct waveform from a SST cell. **b,** Change in voltage with 20 pA current steps for each cell type at P28 or P56. No significant change in excitability was found between age groups (P28, n = 11; P56, n = 9; two-way repeated measures ANOVA followed by Mann-Whitney U, all p values > 0.00625, Bonferroni corrected alpha). **c,** Evoked spiking for all cells before carbachol application (open boxes) and following washout (yellow boxes), for respective cell types. No significant change in response to current injection was found after carbachol application (n = 19; repeated measures ANOVA followed by Wilcoxon signed-rank test, all p values >0.0055, Bonferroni corrected alpha). **d,** Example PV cell waveform. **e,** As in **b**, but for PV cells. No significant change in excitability was found between age groups (P28, n = 8; P56, n = 9; two-way repeated measures ANOVA followed by Mann-Whitney U, all p values > 0.0071, Bonferroni corrected alpha). **f,** As in **c**, but for PV cell responses before and following carbachol washout. No significant change was found (n = 17; repeated measures ANOVA followed by Wilcoxon signed-rank test, all p values > 0.0062, Bonferroni corrected alpha). **g,** Example VIP cell waveform. **h,** As in **b**, but for VIP cells. No significant change in excitability was found between age groups (P28, n = 10; P56, n = 8; two-way repeated

measures ANOVA followed by Mann-Whitney U, all p values > 0.0083, Bonferroni corrected alpha). **i,** As in **c**, but for VIP cell responses before and following carbachol washout. No significant change was found (n = 18; repeated measures ANOVA followed by Wilcoxon signed-rank test, all p values > 0.0083, Bonferroni corrected alpha). Boxplot parameters as in Fig. 1.

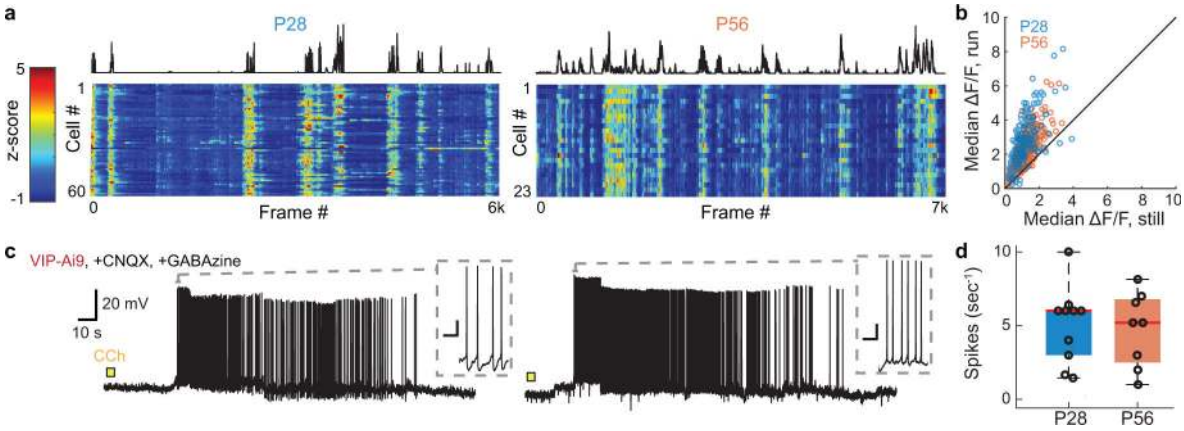

Extended Data Fig. 3 |. VIP cells show no age-dependent changes in cholinergic modulation.
a, As in Figure 1, example VIP cell populations from P28 and P56. **b,** Plot of each cell's visually-evoked median ΔF/F as a function of behavioral state, for all recorded cells (P28, n = 220, still to run, P = 1.63E-64; P56, n = 305, P = 1.75E-60, Wilcoxon signed-rank test). **c,** Example traces of VIP cell response to CCh application at P28 (left) and P56 (right). Recordings were made under current clamp and in the presence of synaptic blockers. Colored box denotes time of CCh application. Insets show evoked VIP cell waveform, scale bars = 0.25 sec, 10mV. **d,** Boxplot of VIP cell firing rates evoked by CCh as a function of age (P28, n = 10, P56, n = 8, P = 0.9804, Mann-Whitney U test). Boxplot parameters as in Fig. 1.

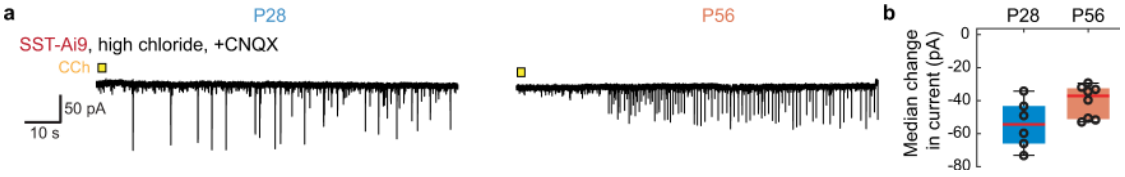

Extended Data Fig. 4 |. CCh-induced IPSCs on SST cells are present across development.
a, Example whole-cell recordings of SST cell responses to CCh in voltage-clamp mode at P28 (left) or P56 (right). **b,** Median IPSC amplitudes evoked by CCh application for all recorded SST cells at P28 and P56 (P28, n = 6, P56, n=8, P = 0.4136, Mann-Whitney U test). Boxplot parameters as in Fig. 1.

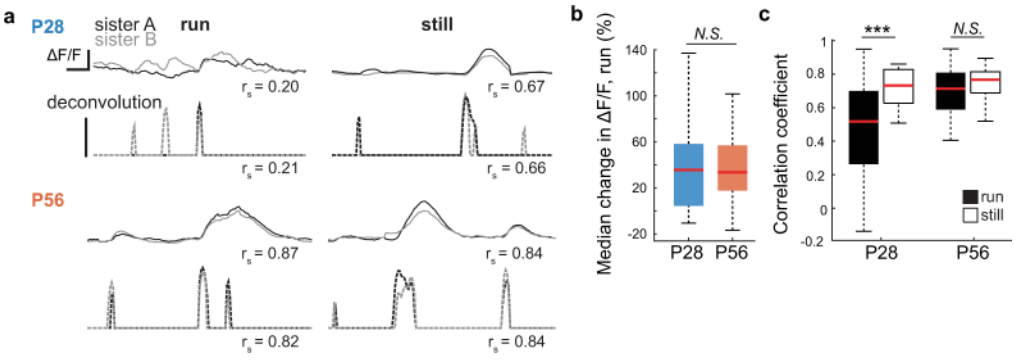

Extended Data Fig. 5 |. Deconvolution and ΔF/F comparisons produce analogous findings in sister dendrites.

a, (Top) A time series showing ΔF/F and concurrent deconvolution for still and run epochs in a sister dendrite from a P28 mouse. Note the deconvolution is based in significant changes in slope. Spearman's correlation coefficients (r_s) are shown. ΔF/F has been filtered for clarity. (Bottom) Same as top for sister dendrites from a P56 mouse. Scale bars are ΔF/F = 1, event probability = 1, a.u., over 1 sec. **b,** Median percent change in ΔF/F from still to run, for all P28 and P56 branches (P28, n = 36 branches, P56, n = 96 branches, P = 0.6608, Mann-Whitney U test). **c,** Correlation of ΔF/F between sister dendrites to movement at P28 or P56. (P28, n = 18 branch pairs, still to run, P = 5.36E-04; P56, n = 48 branch pairs**,** still to run, P = 0.043, Wilcoxon signed-rank test). ***P<0.001, *N.S.* = Not significant. Boxplot parameters as in Fig. 1.

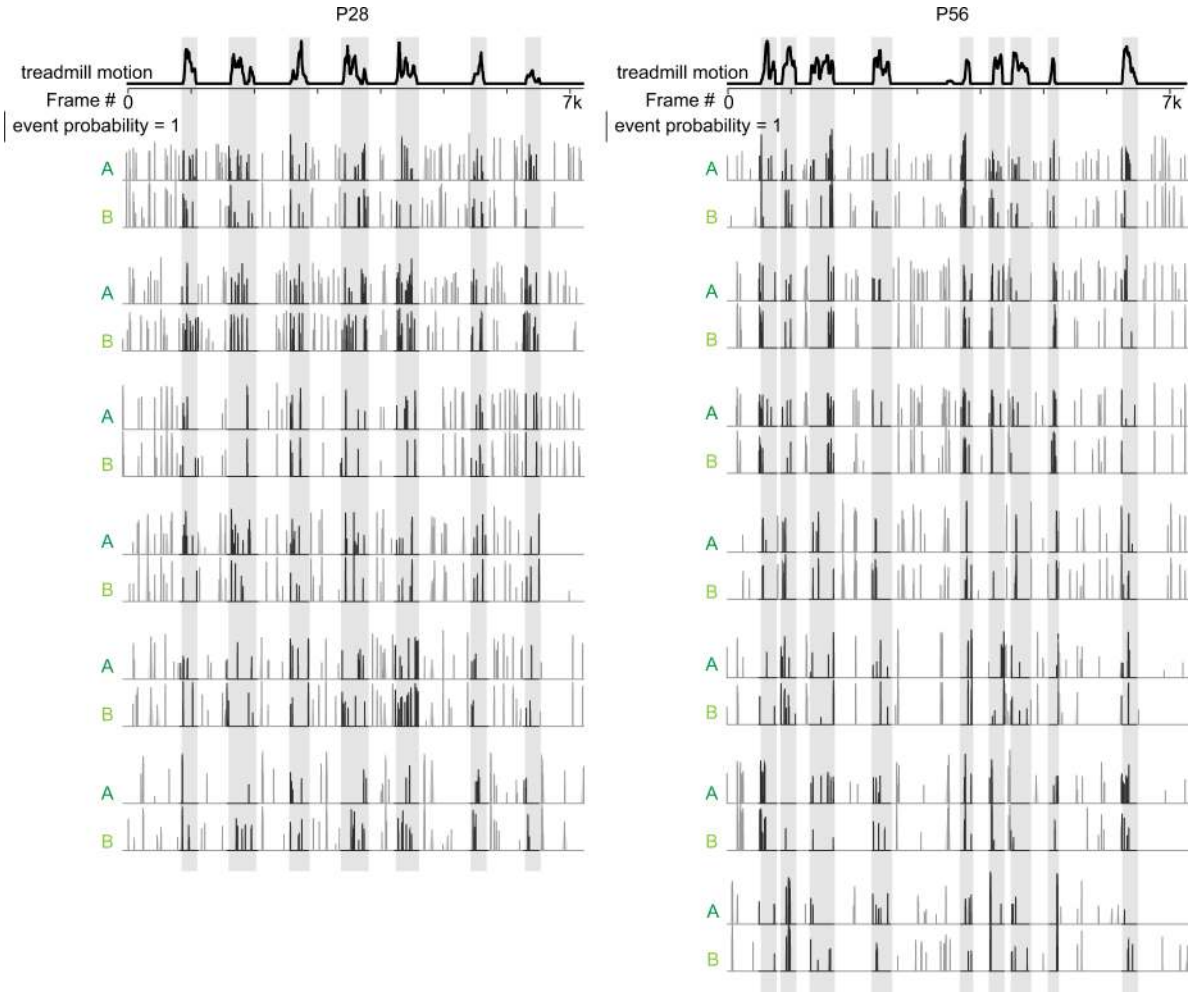

Extended Data Fig. 6 |. Example visually-evoked P28 and P56 sister dendrite activity.
Examples of temporally deconvolved GCaMP6f traces showing event probability in sister dendrites from a P28 and P56 mouse. Gray bars mark periods of locomotion across traces. (Left) P28 sister dendrites show decorrelated activity during movement. (Right) P56 sister dendrites maintain synchronized activity across run and still epochs. Scale bar indicates event probability = 1 a.u.

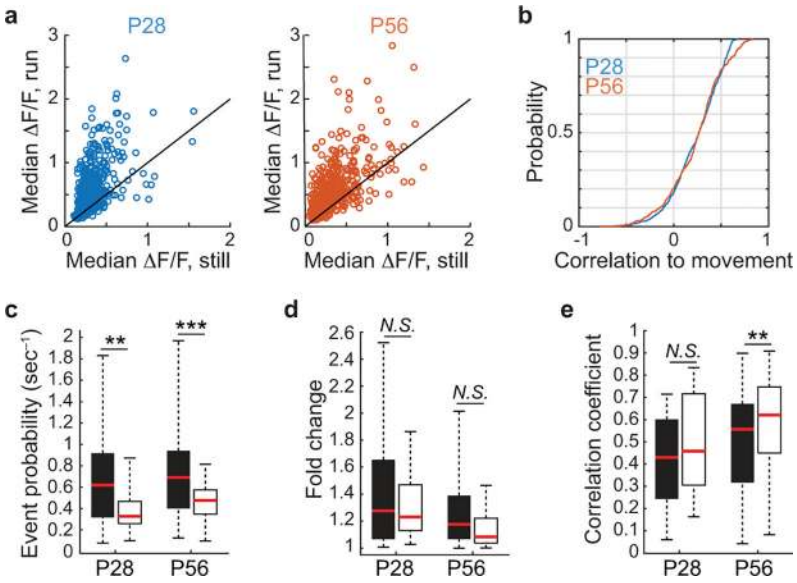

Extended Data Fig. 7 |. P28 and P56 modulation of PYR cell somas and dendrites during spontaneous activity.

a, Plot of each cell's visually-evoked median ΔF/F as a function of behavioral state, for all recorded cells, at P28 and P56, in the absence of visual stimulation, measured at the soma (P28, n = 563 cells, still to run, P = 4.31E-60; P56, n = 723 cells, P = 1.94E-89, Wilcoxon sign rank test). **b,** Plot of cumulative distributions of the correlation coefficients of GCaMP6f signals to running for all recorded pyramidal neurons while viewing a gray screen. (P28: n = 860 cells; P56: n = 513 cells; P = 0.993, Mann-Whitney U test). **c,** Boxplots of temporally deconvolved event probabilities of dendrites during gray screen viewing at P28 and P58 during in running and still conditions. (P28, n = 36 branches; still to run, P = 0.0044; P56, n = 96 branches, still to run, P = 4.36E-06, Wilcoxon sign rank test). **d,** Boxplots of the fold change between sister branches as a function of age and behavioral state (P28, n = 18 branch pairs, P = 0.987; P56, n = 56 branch pairs, still to run, P = 0.02, Wilcoxon sign rank test). **e,** Boxplots of the correlation coefficients between event probability time series of sister branches as a function of age and behavioral state (P28, n = 18 branch pairs, P = 0.2914; P56, n = 56 branch pairs, still to run, P = 0.0042, Wilcoxon sign rank test). **P<0.01, ***P<0.001, *N.S.* = Not significant. Boxplot parameters as in Fig. 1.

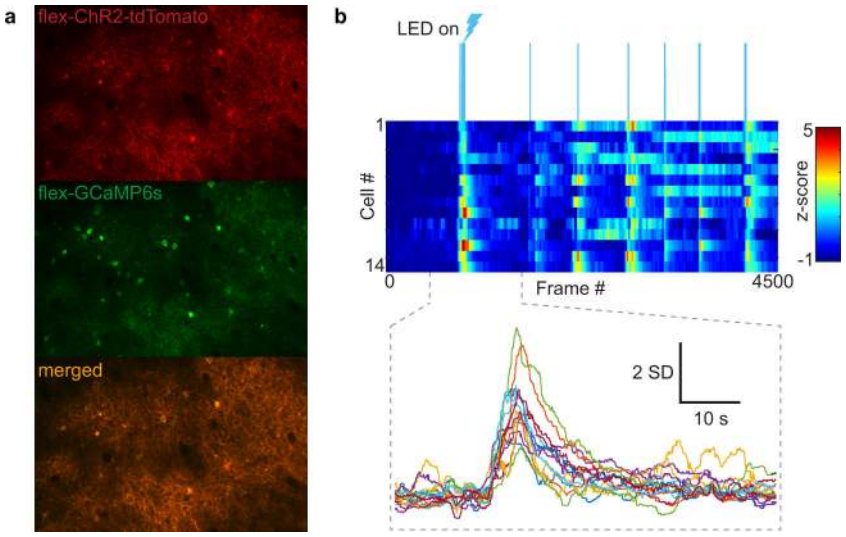

Extended Data Fig. 8 |. Verification of ChR2-driven SST activity *in vivo*.
a, SST cells expressing both ChR2-Tdtomato and GCaMP6s. **b,** Representative time series heat map of SST cell GCaMP6s responses to optogenetic stimulation. Z-scores from individual cells plotted per frame (15.5 fps); color scale is −1 to 5 z-scores. (Top) Blue bars denote LED light pulses. (Bottom) Inset showing z-scored traces and significant increase in GCaMP6 signal for 14 cells.

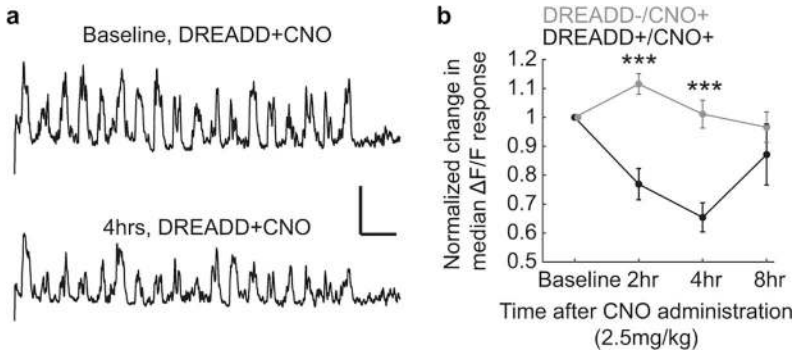

Extended Data Fig. 9 |. Verification of chemogenetic control of SST cells using DREADDs.
a, (Top) Example evoked responses of a SST cell expressing DREADD receptors. (Bottom) Evoked responses from the same SST cell 4 hours after intraperitoneal administration of CNO (2.5mg/kg). **b,** Measurement of change in median evoked ΔF/F in SST cells after CNO administration over an 8 hour period, in animals with or without DREADD expression (DREADD-/CNO+: n = 25 cells, DREADD+/CNO+: n = 21 cells. 2hr, DREADD- to DREADD+: P = 1.41E-04. 4hr, DREADD- to DREADD+: P = 7.98E-05. Wilcoxon signed-rank test). Error bars are S.E.M. ***P<0.001. Scale bar in panel (a) is 10% ΔF/F and 30 sec.

Acknowledgements:

We thank D. Buonomano, P. Golshani, and L. Zipursky for their helpful comments and suggestions. Funding: NIH R01 EY023871 (J.T.T), NIH R01 EY018322 & NIH EB022915 (D.L.R), and NIH F31 EY027196 (C.E.Y.)

REFERENCES

1. Hübener M & Bonhoeffer T Neuronal plasticity: beyond the critical period. Cell 159, 727–737 (2014). [PubMed: 25417151]
2. Froemke RC, Merzenich MM & Schreiner CE A synaptic memory trace for cortical receptive field plasticity. Nature 450, 425–429 (2007). [PubMed: 18004384]
3. Letzkus JJ et al. A disinhibitory microcircuit for associative fear learning in the auditory cortex. Nature 480, 331–335 (2011). [PubMed: 22158104]
4. Cichon J & Gan W-B Branch-specific dendritic Ca(2+) spikes cause persistent synaptic plasticity. Nature 520, 180–185 (2015). [PubMed: 25822789]
5. Kerlin A et al. Functional clustering of dendritic activity during decision-making. BioRxiv (2018). doi:10.1101/440396
6. Spruston N Pyramidal neurons: dendritic structure and synaptic integration. Nat. Rev. Neurosci 9, 206–221 (2008). [PubMed: 18270515]
7. Bear MF & Singer W Modulation of visual cortical plasticity by acetylcholine and noradrenaline. Nature 320, 172–176 (1986). [PubMed: 3005879]
8. Kuhlman SJ et al. A disinhibitory microcircuit initiates critical-period plasticity in the visual cortex. Nature 501, 543–546 (2013). [PubMed: 23975100]
9. Levelt CN & Hübener M Critical-period plasticity in the visual cortex. Annu. Rev. Neurosci 35, 309–330 (2012). [PubMed: 22462544]
10. Crair MC, Gillespie DC & Stryker MP The role of visual experience in the development of columns in cat visual cortex. Science 279, 566–570 (1998). [PubMed: 9438851]
11. Faguet J, Maranhao B, Smith SL & Trachtenberg JT Ipsilateral eye cortical maps are uniquely sensitive to binocular plasticity. J. Neurophysiol 101, 855–861 (2009). [PubMed: 19052109]
12. Wang B-S, Sarnaik R & Cang J Critical period plasticity matches binocular orientation preference in the visual cortex. Neuron 65, 246–256 (2010). [PubMed: 20152130]
13. Wilson DE, Whitney DE, Scholl B & Fitzpatrick D Orientation selectivity and the functional clustering of synaptic inputs in primary visual cortex. Nat. Neurosci 19, 1003–1009 (2016). [PubMed: 27294510]
14. Iacaruso MF, Gasler IT & Hofer SB Synaptic organization of visual space in primary visual cortex. Nature 547, 449–452 (2017). [PubMed: 28700575]
15. Weber JP et al. Location-dependent synaptic plasticity rules by dendritic spine cooperativity. Nat. Commun 7, 11380 (2016). [PubMed: 27098773]
16. Losonczy A, Makara JK & Magee JC Compartmentalized dendritic plasticity and input feature storage in neurons. Nature 452, 436–441 (2008). [PubMed: 18368112]
17. Makara JK, Losonczy A, Wen Q & Magee JC Experience-dependent compartmentalized dendritic plasticity in rat hippocampal CA1 pyramidal neurons. Nat. Neurosci 12, 1485–1487 (2009). [PubMed: 19898470]
18. Tremblay R, Lee S & Rudy B Gabaergic interneurons in the neocortex: from cellular properties to circuits. Neuron 91, 260–292 (2016). [PubMed: 27477017]
19. Gordon JA & Stryker MP Experience-dependent plasticity of binocular responses in the primary visual cortex of the mouse. J. Neurosci 16, 3274–3286 (1996). [PubMed: 8627365]
20. Lee AM et al. Identification of a brainstem circuit regulating visual cortical state in parallel with locomotion. Neuron 83, 455–466 (2014). [PubMed: 25033185]
21. Reimer J et al. Pupil fluctuations track fast switching of cortical states during quiet wakefulness. Neuron 84, 355–362 (2014). [PubMed: 25374359]
22. Chen N, Sugihara H & Sur M An acetylcholine-activated microcircuit drives temporal dynamics of cortical activity. Nat. Neurosci 18, 892–902 (2015). [PubMed: 25915477]
23. Fanselow EE, Richardson KA & Connors BW Selective, state-dependent activation of somatostatin-expressing inhibitory interneurons in mouse neocortex. J. Neurophysiol 100, 2640–2652 (2008). [PubMed: 18799598]
24. Kawaguchi Y Selective cholinergic modulation of cortical GABAergic cell subtypes. J. Neurophysiol 78, 1743–1747 (1997). [PubMed: 9310461]

25. Pfeffer CK, Xue M, He M, Huang ZJ & Scanziani M Inhibition of inhibition in visual cortex: the logic of connections between molecularly distinct interneurons. Nat. Neurosci 16, 1068–1076 (2013). [PubMed: 23817549]

26. Lee S, Kruglikov I, Huang ZJ, Fishell G & Rudy B A disinhibitory circuit mediates motor integration in the somatosensory cortex. Nat. Neurosci 16, 1662–1670 (2013). [PubMed: 24097044]

27. Alitto HJ & Dan Y Cell-type-specific modulation of neocortical activity by basal forebrain input. Front. Syst. Neurosci 6, 79 (2012). [PubMed: 23316142]

28. Cottam JCH, Smith SL & Häusser M Target-specific effects of somatostatin-expressing interneurons on neocortical visual processing. J. Neurosci 33, 19567–19578 (2013). [PubMed: 24336721]

29. Berens P et al. Community-based benchmarking improves spike inference from two-photon calcium imaging data. BioRxiv (2017). doi:10.1101/177956

30. Smith SL, Smith IT, Branco T & Häusser M Dendritic spikes enhance stimulus selectivity in cortical neurons in vivo. Nature 503, 115–120 (2013). [PubMed: 24162850]

METHODS REFERENCES

31. Do JP et al. Cell type-specific long-range connections of basal forebrain circuit. Elife 5, (2016).

32. Gonchar Y, Wang Q & Burkhalter A Multiple distinct subtypes of GABAergic neurons in mouse visual cortex identified by triple immunostaining. Front. Neuroanat 1, 3 (2007). [PubMed: 18958197]

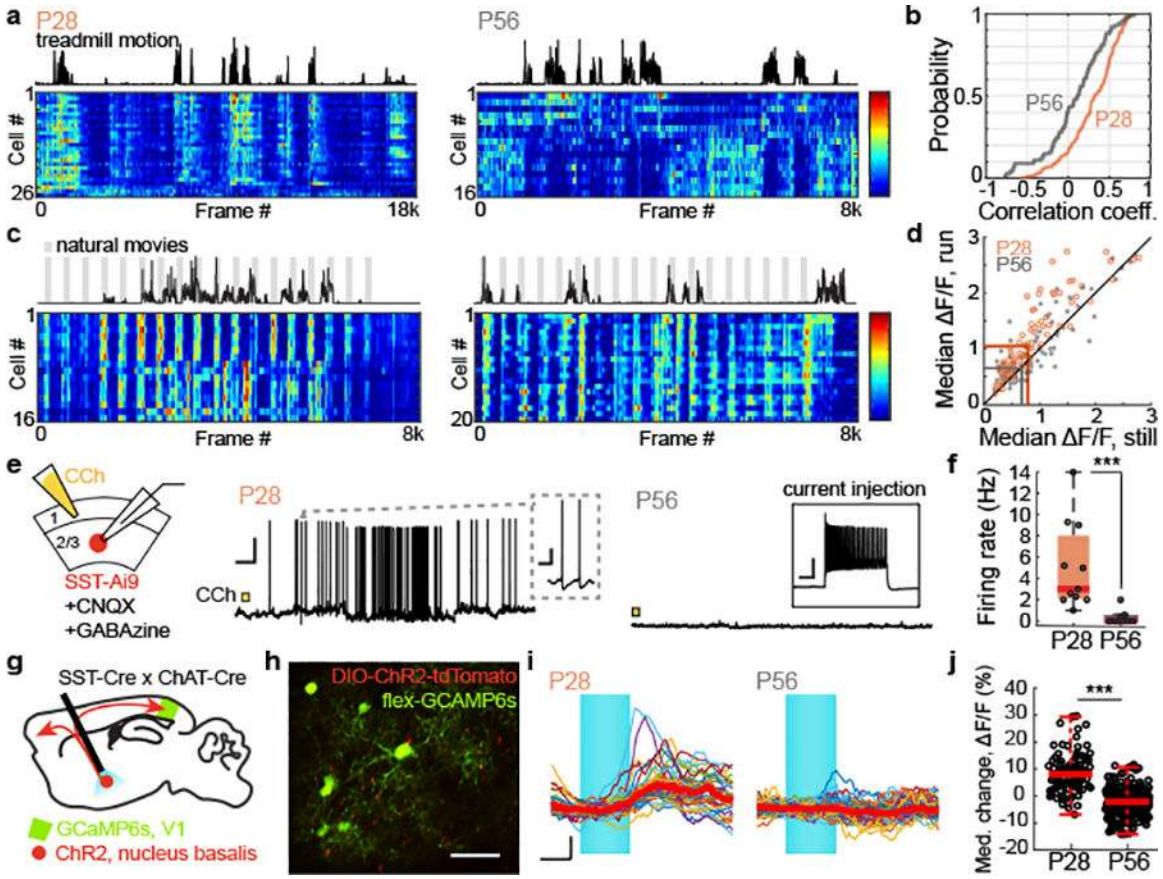

Figure 1. SST cells lose cholinergic sensitivity after critical period closure.

a, Heat map time series of z-scored GCaMP6s spontaneous responses of SST cells recorded in a P28 (left) and a P56 (right) mouse. Scale bar is from −1 to 5.

b, Cumulative distribution of correlation coefficients to running for all SST cells recorded in all mice at P28 (orange) and P56 (gray) (P28: n = 200; P56: n = 100; P = 5.73E-07, Mann-Whitney U test).

c, As in **a**, but for visually-evoked SST responses to non-repeating natural movie scenes. Gray bars indicate times when visual stimulation occurred. Scale bar is from −1 to 4.

d, Plot of each cell's visually-evoked median ΔF/F as a function of behavioral state, for all recorded cells (P28, orange: n = 94, P56, gray: n = 102; P28 run to P56 run, P = 4.63E-06, Mann-Whitney U test).

e, Left, schematic of whole-cell current clamp recordings of SST cell responses to bath application of carbachol (CCh) in the presence of synaptic blockers. Middle, example of responses recorded from a P28 mouse; inset shows evoked SST waveform, scale bar = 0.5 s and 10 mV. Right, example from a P56 mouse; inset shows a healthy response to current injection despite lack of response to CCh, scale bar = 100ms and 20 mV. In both plots, onset of CCh application is denoted by the yellow square. Scale bar is 20 mV and 10 sec.

f, Boxplot of SST cell firing rates evoked by CCh as a function of age (P28: n = 11; P56: n = 9; P = 2.90E-04, Mann-Whitney U test). For these plots, the red central mark denotes the median and the outer edges correspond to the upper and lower percentiles, with whiskers extending to 2σ.

g, Schematic of *in vivo* optical activation of the nucleus basalis with concurrent imaging in V1.

h, V1 SST cells labeled with GCaMP6s and visible ChR2+ butons from the nucleus basalis. Scale bar is 60μm.

i, Representative SST cell activity after nucleus basalis stimulation (blue) in a P28 and a P56 mouse. The median response is shown in red (P28: n = 40; P56: n = 67). Scale bar is 20% ΔF/F and 1 sec.

j, Boxplot of median percent change in ΔF/F for SST cells after nucleus basalis stimulation (P28: n = 101, P56: n = 345; P = 2.89E-33, Mann-Whitney U test). Boxplot parameters as described in **f**.

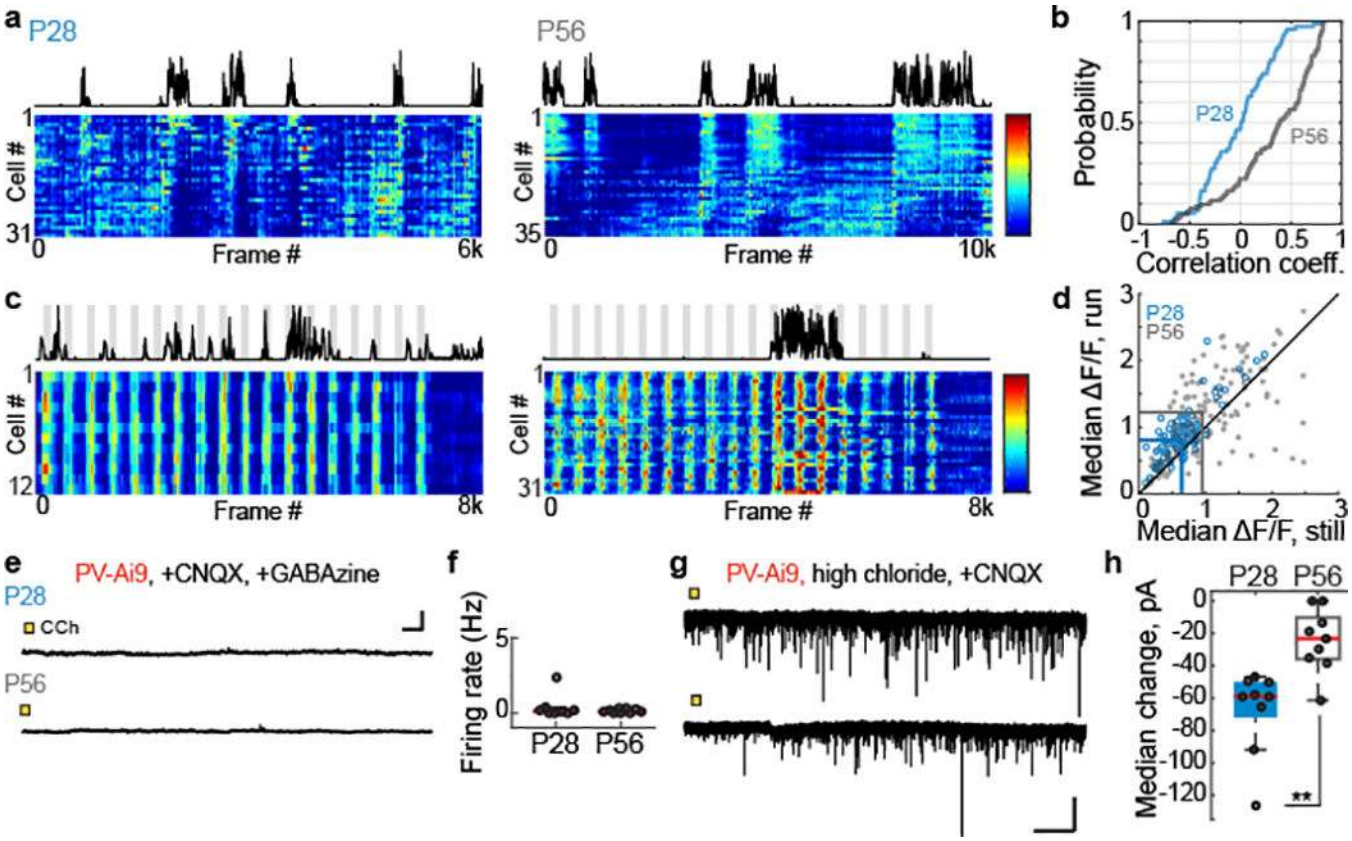

Figure 2. Inhibitory drive onto PV cells weakens after critical period closure.

a, Representative time series heat maps of spontaneous PV cell responses from P28 (left) and P56 (right) mice. Heat map scale bar is in z-score. Scale bar is from −1 to 5.

b, Cumulative distribution of coefficients to running for all recorded PV cells (P28, blue: n = 73; P56, gray: n = 103; P = 3.91E-08, Mann-Whitney U test).

c, As in **a,** but showing PV cell responses to non-repeating natural movie scenes. Heat map scale bar is in z-score. Scale bar is from −1 to 4.

d, Plot of each cell's visually-evoked median ΔF/F as a function of behavioral state, for all recorded cells (P28, blue: n = 101; P56, gray: n = 162; P28 run to P56 run, P = 8.82E-05, Mann-Whitney U test).

e, Example traces of PV cell response to CCh application at P28 (top) and P56 (bottom). Recordings made under current clamp with synaptic blockers. Colored box denotes time of CCh application. Scale bar is 10 mV and 10 sec.

f, Plot of CCh-evoked responses for all PV cells recorded in slices taken from P28 and P56 mice (P28: n=8; P56: n=9; P = 0.8346, Mann-Whitney U test).

g, Examples of voltage-clamped whole cell recordings of PV cell responses to bath application of CCh at P28 (top) or P56 (bottom). Scale bar is 50 pA and 10 sec.

h, Plot of median IPSC amplitude evoked by CCh application for all recorded PV cells at P28 and P56 (P28: n = 9; P56: n = 9; P = 0.0012, Mann-Whitney U test).

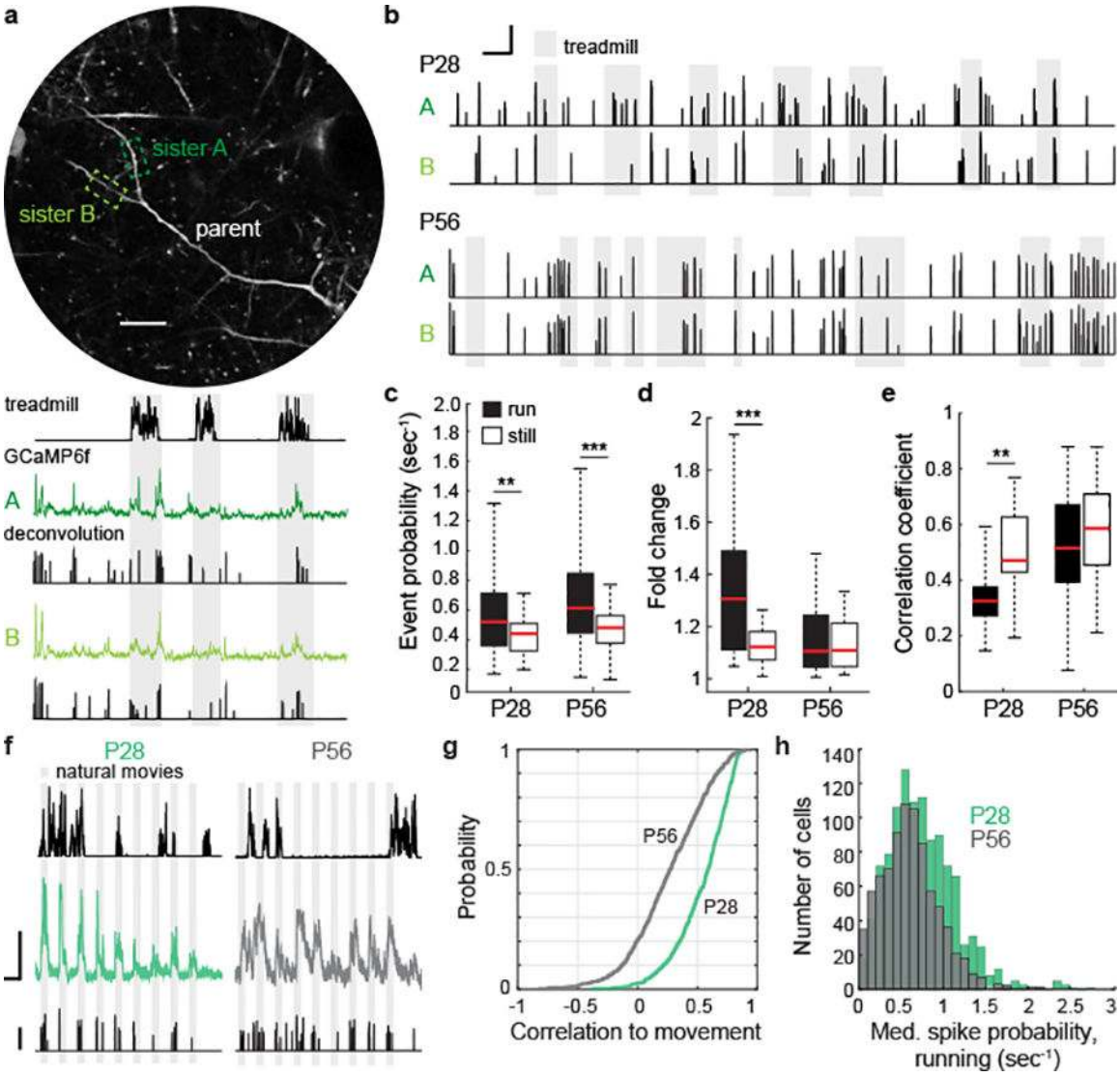

Figure 3. Movement evokes branch-specific Ca^{2+} spikes in apical L2/3 dendrites and increased somatic firing during the critical period.

a, Representative sister dendrites from a P28 mouse expressing GCaMP6f with corresponding time-series of calcium signals, deconvolution, and treadmill motion (below). Scale bar is 20μm. Gray bars mark periods of locomotion.

b, Examples of temporally deconvolved GCaMP6f traces showing event probability in sister dendrites from a P28 and P56 mouse. Scale bar is 20 seconds, event probability = 1 a.u.

c, Boxplot of event probability by state and age (P28, n = 36 branches, P = 0.0128; P56, n = 96 branches, P = 4.19E-05, Wilcoxon signed-rank test).

d, Boxplots of absolute value of the log-transformed change in event probabilities between sister branches by age and state (P28, n = 18 branch pairs, P= 0.007; p56, n = 48 branch pairs, P=0.79, Wilcoxon signed-rank test).

e, Boxplots of correlation coefficients between event probability time series in sister branches (P28, n = 18 branch pairs, P = 0.0104; P56, n = 48 branch pairs, P = 0.05, Wilcoxon signed-rank test).

f, Example responses to visual stimulation from a pyramidal cell soma at P28 (left) and P56 (right). For each age, 3 time series plots are shown: locomotion plotted at the top, z-scored GCaMP6f response in the middle, and the temporally deconvolved spike probability at the bottom. Scale bars for GCaMP6f signals are 20s and 2 S.D. Deconvolved spike probability scale bar = 1 a.u.

g, Plot of cumulative distributions of the correlation coefficients of GCaMP6s signals to running for all recorded pyramidal neurons (P28, green: n = 1187; P56, gray: n = 821 cells; P = 5.03E-82, Mann-Whitney U test).

h, Histogram of median spike probability per second measured during running in P28 (green) and P56 (gray) mice (P28: n = 1187; P56: n = 821; P = 0.0114, Mann-Whitney U test).

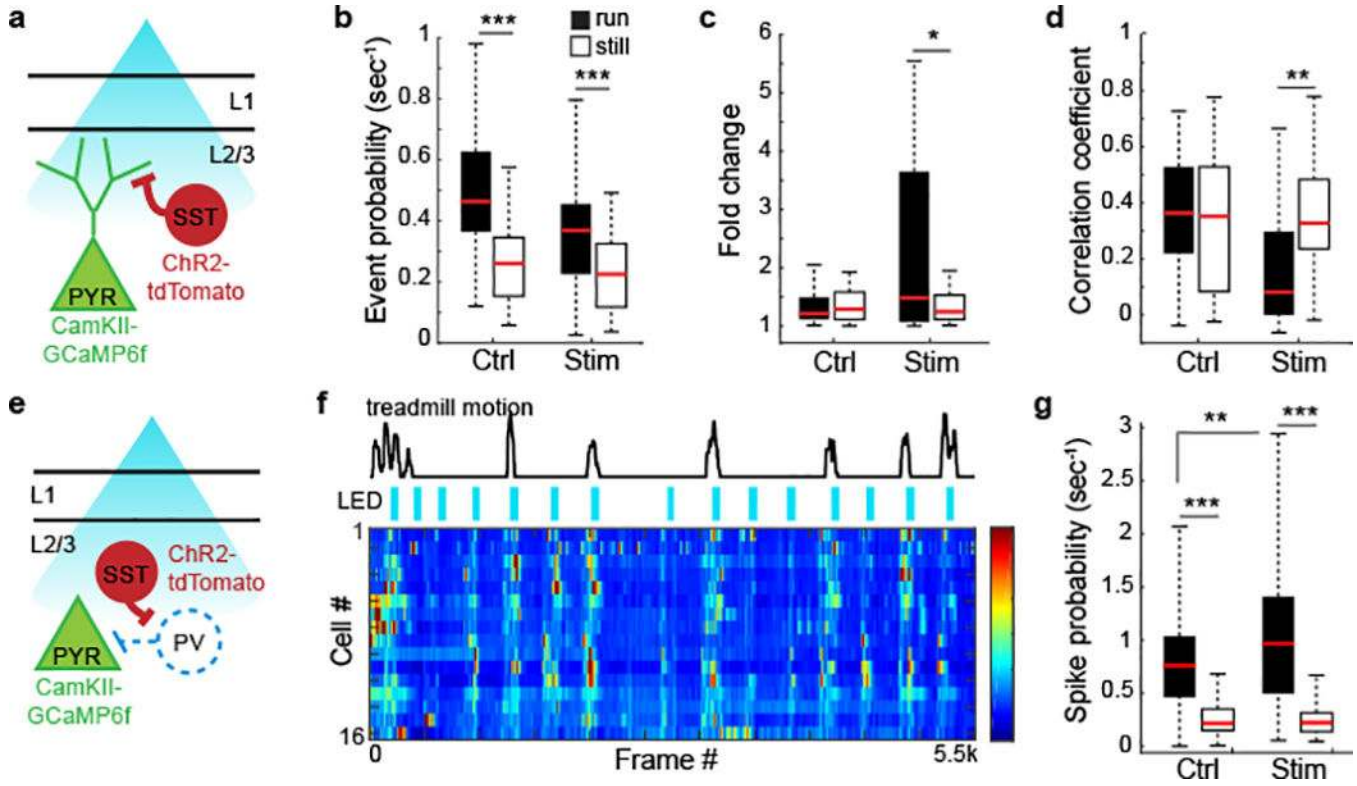

Figure 4. Optogenetic stimulation of SST cells increases compartmentalized dendritic responses and somatic firing in P56 mice.

a, Schematic of optogenetic setup.

b, Boxplots of temporally deconvolved event probabilities of dendrites in P56 mice recorded during before (control) and during (stim) blue light stimulation trials in running and still conditions (n = 82 branches; control still to run, P = 4.16E-05; stim still to run, P = 4.96E-10, Wilcoxon signed-rank test).

c, Boxplots of the absolute value of the log-transformed change between sister branches as a function of SST optogenetic stimulation and behavioral state (n = 41 branch pairs; control still to run, P = 0.2735; stim still to run, P = 0.0232, Wilcoxon signed-rank test).

d, Boxplots of the correlation coefficients between event probability time series of sister branches as a function of SST optogenetic stimulation and behavioral state (n = 41 branch pairs; control still to run, P = 0.9535; stim still to run, P = 0.0044, Wilcoxon signed-rank test).

e, As in **a**, with the exception that pyramidal cell somas are recorded.

f, Representative time series heat map of pyramidal cell responses in a P56 mouse with optogenetic stimulation of SST cells. Z-scores from individual cells plotted per frame (15.5 fps); color scale is −1 to 5 z-scores. Top, black trace denotes locomotion; blue bars denote optogenetic stimulation.

g, Boxplots of somatic spike probabilities as a function of behavioral state in P56 mice before (control) or during (stim) optogenetic SST cell stimulation (n = 79; control still to run, P = 1.14E-11, stim still to run, P = 1.10E-11, stim run to control run, P = 6.00E-03, Wilcoxon signed-rank test with post-hoc Bonferroni correction).

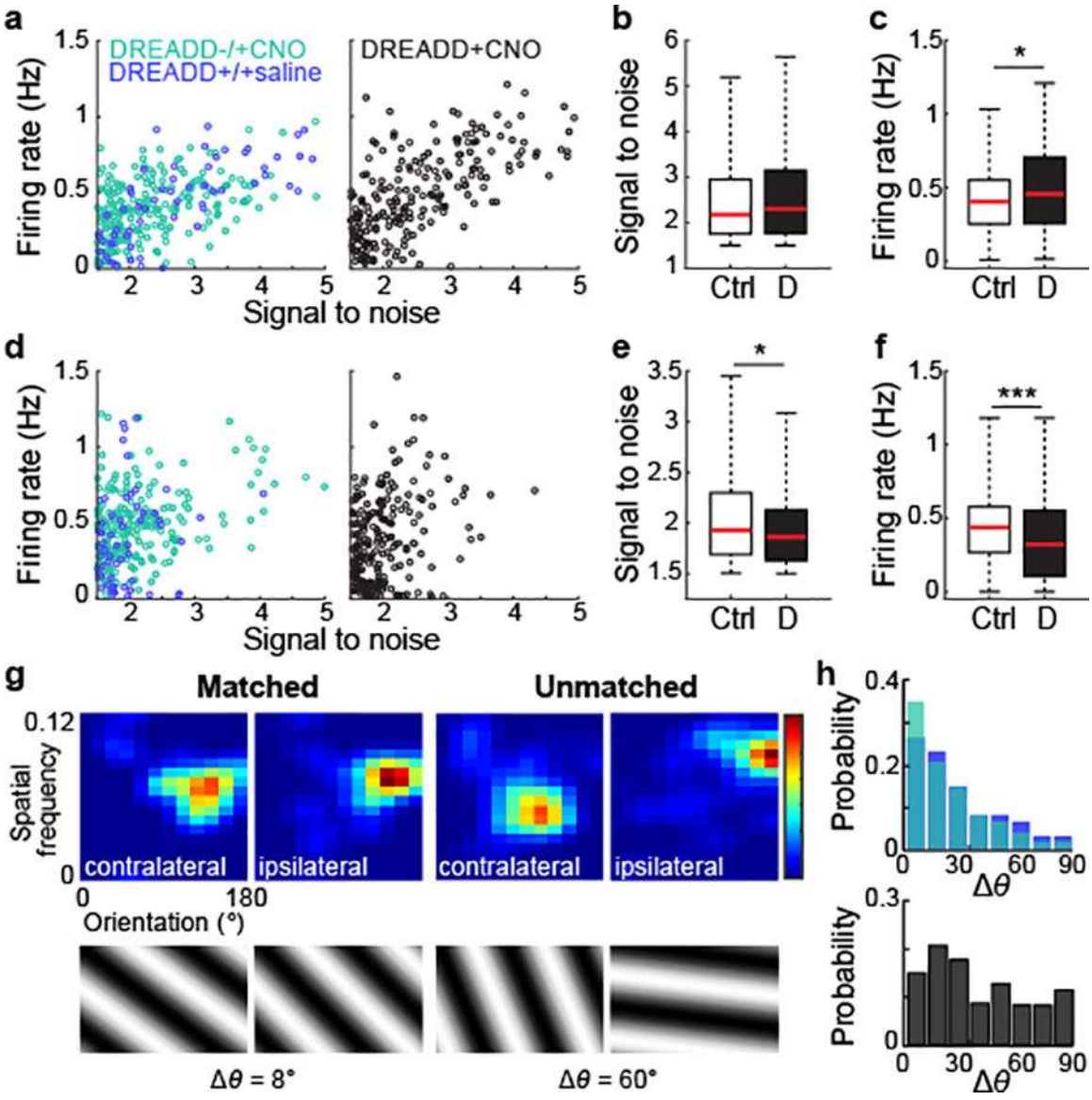

Figure 5. Suppression of SST cells during the critical period prevents binocular matching.

a, Contralateral response properties of all recorded binocular neurons in P28 mice, from control groups (left) or mice with DREADD-mediated SST cell suppression prior to recording (right). Plots are of deconvolved firing rate and the signal-to-noise ratio of the contralateral receptive field (DREADD−/+CNO, n = 223 cells; DREADD+/+saline, n = 60 cells; DREADD+CNO, n = 226 cells).

b, Boxplots of the signal-to-noise ratios of contralateral receptive fields for either pooled controls or the experimental group (Controls, n = 283 cells, DREADD, n = 226 cells, P = 0.3520, Mann-Whitney U test).

c, Boxplots of the inferred firing rate of contralateral responses in control or experimental groups (Controls, n = 283 cells, DREADD, n = 226 cells, P = 0.0145, Mann-Whitney U test).

d, As in **a**, but for ipsilateral responses.

e, As in **b**, but for ipsilateral receptive fields for either control or experimental groups (Controls, n = 283 cells, DREADD, n = 226 cells, P = 0.0234, Mann-Whitney U test).
f, As in **c**, but for ipsilateral responses in control or experimental groups (Controls, n = 283 cells, DREADD, n = 226 cells, P = 1.1637E-4, Mann-Whitney U test).
g, Example binocular neurons showing matched (left) or unmatched (right) receptive fields. Plots are individually normalized to show the maximum response in the spatial frequency (cycles per degree) and orientation (degrees) domains. Discrepancy in preferred orientation in degrees ($\Delta\theta$) is noted.
h, Histograms of probability distribution of $\Delta\theta$ in binocular neurons in control (top) and experimental (bottom) groups. (Controls, n = 283 cells, DREADD+CNO, n = 226 cells, P = 2.67E-10, Mann-Whitney U test).